On the use of PIV, LII, PAH-PLIF and OH-PLIF for the study of soot formation and flame structure in a swirl stratified premixed ethylene/air flame

Maxime Bouvier, Gilles Cabot, Jerôme Yon, Frederic Grisch

On the use of PIV, LII, PAH-PLIF and OH-PLIF for the study of soot formation and flame structure in a swirl stratified premixed ethylene/air flame

Maxime Bouvier[a], Gilles Cabot[a], Jérôme Yon[a], Frédéric Grisch[a,*]

[a]*Normandie Univ, UNIROUEN, INSA Rouen, CNRS, CORIA, 76000 Rouen, France*

Colloquia: **Diagnostics**, Alternative: Gas turbine and Rocket engine combustion

Total length of the paper : 6195 words

Part	Equivalent word length
Main text	4199
References	489
Table 1	68
Figure 1 + caption (1 column)	151
Figure 2 + caption (2 columns)	299
Figure 3 + caption (2 column)	369
Figure 4 + caption (1 columns)	122
Figure 5 + caption (2 columns)	281
Figure 6 + caption (1 columns)	217
Total	6198

Supplemental materials available.

[*]*Corresponding author*

Email address: frederic.grisch@coria.fr

Abstract

Soot formation and oxidation are investigated in swirl stratified premixed ethylene/air flames at atmospheric pressure. The effects of both swirl and stratification are studied to understand the relationship between the flame structure, soot precursors and soot. The topology of the flame is obtained with particle image velocimetry (PIV) and planar laser-induced fluorescence (PLIF) on hydroxyl radical (OH). The production of polycyclic aromatic hydrocarbons (PAHs) is investigated using PLIF by mainly probing the aromatic compounds with two benzene rings (i.e. naphthalene) that are known to actively participate in soot nucleation and growth. Soot production is investigated using laser-induced incandescence (LII), giving quantitative data on the soot volume fraction. Extensive information on the flame structure and the mechanisms of formation/consumption of soot is gathered based on the coupling of these laser diagnostics. An image analysis of velocity, OH, PAHs and soot distributions enables us to propose a scenario that describes the link between the inception, growth, aggregation and oxidation processes. In particular, the data reveal the presence of distinct zones for these processes: a thermal decomposition region in which PAHs contributes to nascent soot formation, organised as filaments along the interface between the PAH region and the inner recirculation zone (IRZ); a mixing region controlled by large moving structures that favour the growth and aggregation of nascent soot into mature soot; and an oxidation region leading to the fast consumption of soot particles. These processes are impacted to varying extents by the intensities of swirl and stratification.

Keywords

Soot, PAHs, OH, swirl stratified flame, LII/LIF

1. Introduction

For a long time, the effect of soot particles on the environment was considered to be negligible compared with greenhouse gases such as CO_2 and CH_4. However, recent studies have shown that soot emissions have a severe impact on global warming, to the point that they are now considered the second highest anthropogenic contributor to radiative forcing, just behind CO_2 [1]. In the field of transportation, aircraft engine emissions were estimated to be the second largest contributor in 2015 [2]. For these reasons, stringent regulatory standards concerning soot emission will come into effect in the future years. In consequence, aircraft engine manufacturers have to develop innovative combustion systems with the aim of reducing fuel consumption and soot emissions while maintaining a high combustion efficiency. Over the years, lean premixed swirl combustion has become a valuable approach to meet these regulations. However, the technology associated with this concept may produce flame instability, partial extinction or low reaction rates [3, 4]. To tackle these limitations, manufacturers of aircraft engines have developed promising technologies based on partially premixing and stratifying the reaction mixture to obtain better flexibility of control of flame stability, over a large range of operating conditions. Several investigations have previously been performed to study the flame structure of academic premixed swirl and stratified flame topologies [5, 6]. These studies have produced detailed information on the benefits of local mixture fraction gradients on the increase in heat release from globally fuel-lean combustion and the larger flame structure sensitivity to the specific inlet fuel-air distribution. Perhaps surprisingly, no data are available on the impact of swirled and stratified flames on the reduction of NOx and soot emissions, unlike in the case of fully premixed swirl flames in which joint numerical and experimental studies have given a detailed understanding of soot formation and oxidation [7-9].

In the context described above, a detailed investigation is required on how variations in swirl and stratification affect soot formation. The study of soot production and consumption is a complex task since the mechanisms involved are dependent on numerous parameters. Firstly, the thermal decomposition of fuel, via several chemical reactions and under suitable thermophysical conditions, forms polycyclic aromatic hydrocarbons (PAHs) [10]. PAHs are then transformed in solid particles via the nucleation process [11]. Surface growth and aggregation finally produce aggregates of 10 to 50 nm diameter primary particles. These growth mechanisms also compete with oxidation caused by chemical reactions between oxygenated compounds and the soot surface, which offer a way of consuming soot particles [12]. These mechanisms must be identified in order to gain an accurate understanding of soot production, and this can be achieved by performing in-situ optical measurements [13].

This work presents results on the formation of soot in swirl stratified premixed C_2H_4/air flames. This is accomplished by simultaneously imaging the velocity, the soot volume fraction, and the distributions of hydroxyl radical (OH) and PAHs, using particle image velocimetry (PIV), laser-induced incandescence (LII), and OH and PAH planar laser-induced fluorescence (PLIF), respectively. A combination of these diagnostics is shown to provide an in-depth understanding of the physical processes governing soot formation in swirl stratified flames. The links between soot, OH and precursors, highlighting the combined effects of the flame structure, the intermittency of soot formation and aerodynamics are discussed.

2. Experimental setup

2.1. Burner configuration

Experiments were performed on the laboratory burner called SIRIUS (SwIrl stRatIfied bUrner for the study of Soot production), which produces variable swirl and stratified premixed flames at

atmospheric pressure. The burner, shown in Fig. 1, has an architecture similar to that of the Sandia/Cambridge burner [6]. The base of the burner consists of three concentric tubes (with diameters 10, 20 and 29.5 mm) in a laminar co-flow, where the central tube is sealed with a ceramic cap acting as a bluff body for flame stabilisation. Two independent fuel/air injection circuits are used (inner and outer annuli) to enable the injection of premixed ethylene/air flows at specific equivalence ratios. The outer annulus is designed to perform experiments with or without swirl flows.

The operating conditions are summarised in Table 1. The stratification ratio (SR) is defined as the ratio between the nominal equivalence ratios in the inner flow (Φ_i) and the outer flow (Φ_o). The swirl flow ratio (SFR) denotes the ratio of the outer flow rate through the swirl plenum ($\dot{m}_{o,radial}$) to the total outer annulus flow ($\dot{m}_{o,axial} + \dot{m}_{o,radial}$). These definitions follow those in [6, 14].

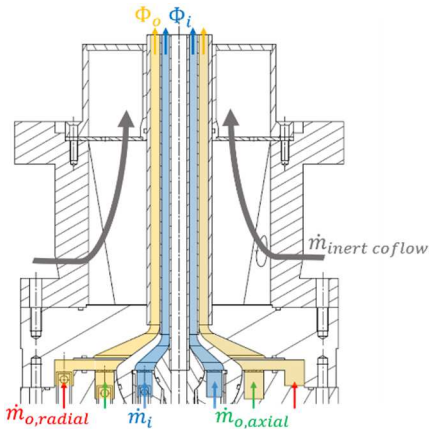

Figure 1: Swirl stratified premixed burner.

SR is varied from 2.1 to 3, while SFR ranges between 0.2 (for less swirling flows) to 0.3 (for highly swirling motion). These values correspond to a swirl number (S) of between 0.31 and 0.63. They were calculated as the ratio of the measured mean tangential velocity to the axial velocity, above the centre of the outer annulus, and were obtained from PIV measurements. The global equivalence ratio $\Phi_g = (\Phi_i + \Phi_o)/2$, the inner mass flow rate $\dot{m}_i$ and the total outer mass flow

rate $\dot{m}_o$ remain fixed for all operating conditions: $\Phi_g = 1.45 \pm 0.03$, $\dot{m}_i = 0.69\ g.s^{-1}$, $\dot{m}_o = 4.2\ g.s^{-1}$. This results in Reynolds numbers of 6000 for the outer flow and 1800 for the inner flow. Finally, the total power load P varies from 10.6 kW for highly stratified cases to 15.6 kW for the others.

Case	Φ_i	Φ_o	SR	SFR
1	2.21	0.74	3.00	0.20
2	2.21	0.74	3.00	0.25
3	2.21	0.74	3.00	0.30
4	1.96	0.93	2.10	0.20
5	1.96	0.93	2.10	0.25
6	1.96	0.93	2.10	0.30

Table 1 : Operating conditions.

2.2. Simultaneous OH- and PAH-PLIF, PIV and 2D-LII measurements

Several techniques are used simultaneously: OH-PLIF is applied to study the combustion reaction, PAH-PLIF to assess the chemical decomposition of the fuel into aromatics, 2D-LII to visualise soot particles and two-component PIV to characterise the aerodynamics.

The laser source used for the OH-PLIF, PAH-PLIF and 2D-LII measurements was a dye laser circulating Rhodamine 590 dissolved in ethanol, pumped by a Nd:YAG laser generating pulses at 532 nm with a duration of 6 ns and a repetition rate of 10 Hz. The output of the dye laser was frequency-doubled to deliver laser pulses at a wavelength of 282.75 nm, in order to simultaneously excite the $Q_1(5)$ rotational line of the OH $A^2X^+(0,0) \leftarrow X^2\Pi(0,1)$ electronic band, the PAH molecules (mainly mono- and di-aromatics) and the soot particles. The $Q_1(5)$ transition was chosen due to its potential to deliver fluorescence with high intensity, well-isolated spectral features and low temperature dependence [15]. The pulsed beam at the laser exit was transformed into a

collimated laser sheet 50 mm high, using a set of cylindrical and spherical lenses. The beam energy (3-4 µJ per ~50 X 50 x 200 μm^3 volume element imaged by each pixel of the camera) was kept well below the measured limits of the linear OH- and PAH-fluorescence regimes [16, 17], but was sufficient to obtain LII signals with a good SNR. Two 16-bit emICCD cameras (Princeton Instruments) were used: one for OH fluorescence and the other for PAH-PLIF and LII signals. The two cameras were located at opposite sides of the laser sheet: one was oriented at right angle while the other was slightly tilted to allow the PIV camera to be oriented perpendicular to the laser sheet. Each camera had a CCD array of 1024x1024 pixels and was equipped with a 100 mm, f/2.8 UV-objective. For OH measurements, the camera was equipped with WG295 and UG11 coloured glass filters, combined with a dichroic filter centred at 315 nm (FWHM = 15 nm). For the PAH/soot measurements, coloured and long-pass optical filters enabled the collection of PAH fluorescence signals above 325 nm, the domain in which LII signals and the fluorescence of aromatics (mainly naphthalene, and to a lesser extent, some higher molecular mass PAHs) are detected [18]. The exposure time used for OH detection was fixed at 50 ns, while a 100 ns temporal gate was used for the PAH/soot camera. This value was selected to integrate the major part of the LII temporal signal while minimising the luminosity of the flame. This procedure gave LII signals that were much larger than the PAH fluorescence signals, with typically one order of magnitude of difference between both signals. It also provided a convenient way of separating the PAH and LII signals in single-shot PAH/soot images (see Fig. 4, which shows PAH/LII images recorded at two different heights). A thresholding image processing procedure base on the triangle method [19] and detailed in the supplemental materials was applied to isolate these contributions in single-shot images.

The PIV excitation system was a double-pulse Nd:YAG laser (Evergreen) operating at 532 nm, which produced pulse pairs (interpulse time = 10 µs) at a frequency rate of 10 Hz. A combination of PIV and PLIF experiments was realised by inserting the PLIF laser pulse between the two PIV laser

pulses. The green laser beam was combined with the UV beam using the same optical lenses to produce a 2D laser sheet, 0.2 mm thick and 50 mm high, positioned on the axis of symmetry of the flame. Both the inner and outer streams were seeded with ZrO_2 particles using a home-made cyclone seeder. Particles illuminated by the green laser beams were imaged using a double frame CCD camera (Jai TM4200CL, 2048 × 2048 pixels). The PIV vectors were obtained by cross-correlation of the PIV images using the Dynamic Studio software (Dantec Dynamics) with final interrogation windows of 8 × 8 pixels, yielding a single velocity vector measurement on a 2D grid with $200\ \mu m$ spacing.

2.3. Laser-induced incandescence

Although the methodology described in the previous section enables a correlation between the instantaneous fields of the PAHs, OH and soot particles, it does not provide quantitative information on soot particles. Moreover, measurement of the soot volume fraction measurement by LII requires the full removal of PAH signals and suitable calibration. The quantitative soot results were obtained from the application of 2D-LII diagnostic. The experimental setup used a Nd:YAG laser to deliver a laser pulse of 6 ns duration at 1064 nm with energy 160 mJ. The beam was converted to a laser sheet 50 mm high and 500 µm thick providing a laser fluence of 0.32 J/cm² at the probe volume. A camera equipped with a bandpass filter enabled the detection of soot incandescence in a spectral interval of 350-400 nm. Calibration of measurements was performed in a laminar sooting flame produced by a McKenna burner, using the extinction technique at 1064 nm [20] and adopting a value of 0.37 for the absorption function $E(m)$ (mature ethylene soot [21]).

3. Results and discussion

3.1. Flow field structure

Simultaneous single-shot measurements of PIV, OH-PLIF, PAH-PLIF and LII were made at two heights above the burner (HAB), and were assembled. The results shown in Fig. 2 were obtained for cases 1 to 3. In each image, the left-hand side shows instantaneous images of the velocity, OH, PAH and soot distributions, while the right side displays the time-averaged distributions.

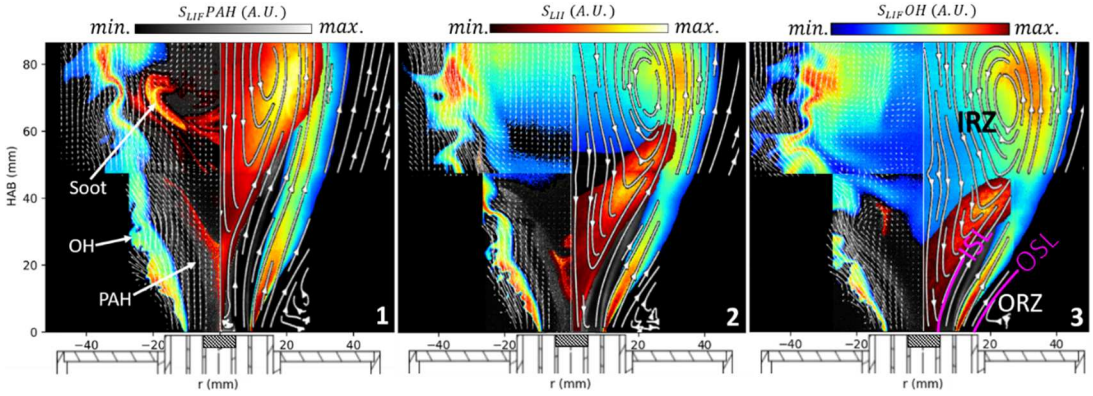

Figure 2: Combined instantaneous (left) and time-averaged (right) images of velocity, OH-PLIF, PAH-PLIF and soot distributions. The velocity vectors (instantaneous) and streamlines (time-averaged) represent the axial and radial components.

The flame structures are typical of swirl stabilised turbulent flames. Using a time-averaged approach, the geometry of the flows consists of an inner recirculation zone (IRZ), which is stabilised by the bluff body, a weak outer recirculation zone (ORZ), an annular jet flow with a higher velocity that separates the IRZ and ORZ, and two annular shear layers, the outer shear layer (OSL) and the inner shear layer (ISL). Time-averaged velocity fields show values of about 1 $m.s^{-1}$ for the IRZ, 5 $m.s^{-1}$ for the inner flow and 15 $m.s^{-1}$ for the outer flow. Each shear layer arises from the large gap between the velocities of the inner/outer flows and the recirculation flows, which generates large velocity fluctuations and large coherent structures that are easily observable in the instantaneous 2D flow velocity displayed in Fig 2. A comparison of the three time-averaged velocity distributions shows that the increase in the swirl significantly modifies the vortex structure inside the IRZ in terms of its shape, size and intensity. The time-averaged velocity distribution offers little information that can contribute to an understanding of the interaction between the aerodynamic

flow and soot formation, since dynamic phenomena such as turbulence or local equivalence ratio gradients play an important role in the production of soot. A detailed analysis of the instantaneous distributions (Fig. 2) shows the effects of swirl in terms of the modification of flow parameters such as turbulence and the transportation of fresh and/or burnt molecular species, which have a strong impact on the formation and oxidation of soot particles. This point will be discussed in the following sections.

3.2. Flame, PAH and soot structures

Overlay images for OH and PAHs are shown in Fig. 3, for two stratifications and three swirl conditions. In each image, the left-hand side shows instantaneous images of OH-PLIF and PAH-PLIF distributions, while the right-hand side shows time-averaged images. All instantaneous images used for the averaging were background subtracted and corrected for laser-sheet intensity variations by performing acetone-LIF in a homogeneously filled cuvette. As for all 2D measurements in turbulent flows, out-of-plane motion can impact the analysis. Particular care was taken when analysing the instantaneous images to check that the observations were applicable to a large sample of images, in order to reduce the impact of 3D structures. Under all conditions, OH exists as a continuous layer, of which the gradient is considered a marker of the flame front. The images show that the flame is anchored at the lip of the pipe separating the inner and outer premixed fuel/air streams. OH is abundantly present in the reaction zone, and its highest fluorescence intensity is observed along the flame front.

For weakly swirling flames (shown in the left-hand columns in Fig. 3), the OH distributions indicate that the flame is mainly propagating without expansion, while the flame edges developing in the lean region (outer region) show large-scale undulations and corrugations. No presence of OH radicals in the centre of the flame is observed, demonstrating an absence of shear layer flames in

the rich side of the flame (inner region). Increasing the swirl number modifies the expansion of the flame. The flame progressively opens with an increase in swirl, due to the larger penetration of combustion products inside the IRZ. This effect is easily discernible from OH-PLIF images collected with SFR = 30%, in which a significant amount of OH appears in the centre of the flame. As already observed for weak swirl flames, the existence of a large equivalence ratio in the centre part of the flame prevents any development of the flame front.

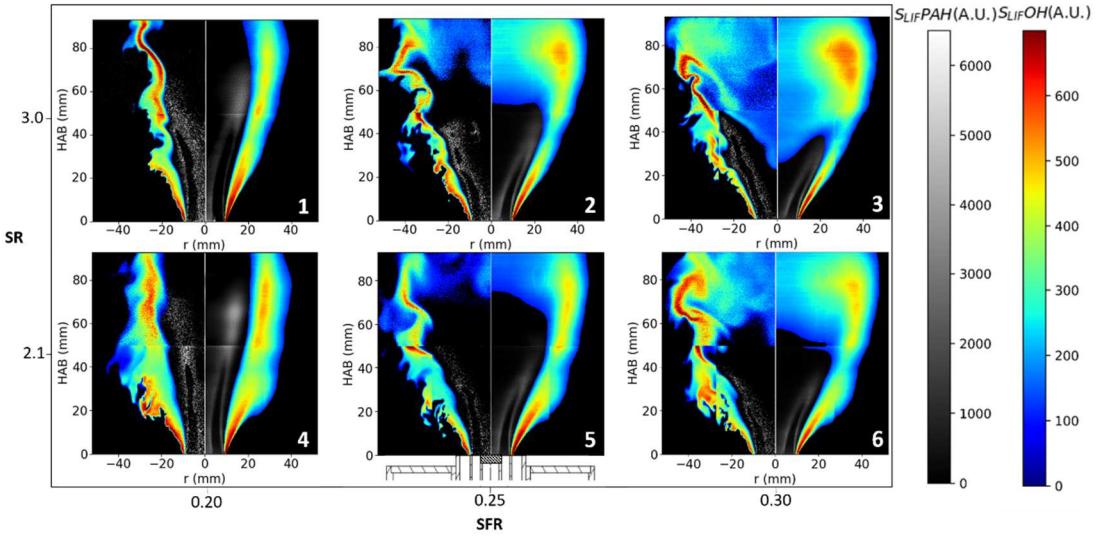

Figure 3: Combined instantaneous (left) and time-averaged (right) images of OH-PLIF (colour) and PAH-PLIF (greyscale) images.

In contrast to the OH images, the instantaneous and averaged PAH-PLIF distributions reveal that PAHs are formed along the inner fresh fuel/air stream (represented by a thin dark zone in the images) and are slightly spread in a radial direction. These results clearly indicate that the ethylene fuel injected by the inner tube is thermally decomposed into sub-products that are involved in the formation of PAH [22]. No PAH fluorescence signals are detected in the thin region located between the flame front and the boundary limit of the PAH zone. These aromatics may be oxidised when they meet oxidizing species and the high temperatures induced by proximity with burnt gases.

Regarding the effects of the swirl and stratification, the height at which PAHs are destroyed is correlated with the topology of the flames. Low swirl numbers (cases 1 and 4) lead to the presence of PAHs at large heights (~ 60 mm), whereas they are only detected at lower heights (~ 40 mm) for larger swirl numbers. As highlighted by the OH distributions, the presence of PAHs at large HAB is strongly correlated with the recirculation of hot combustion products in the IRZ. The larger the swirl number, the higher the efficiency of penetration of hot products such as OH into the core of the flame. Since OH is one of the main species involved in the PAH oxidation process [10], its presence at lower heights will prevent small PAHs from growing into larger aromatics. This observation is supported by the fact that no overlay of OH and PAHs is observed in the single-shot combined images.

Figure 4 shows two instantaneous LII images under condition 1 in the lower (left) and upper (right) part of the flame, overlaid with PAH-PLIF images. It should be noted that these LII images are typical for approximately 90% of the dataset. From Fig. 4, it is evident that PAHs are produced upstream of any measurable soot in the flame. Signals from soot LII occur in two specific regions, revealing different steps in the formation of soot from “nascent” to “mature” soot particles. Here, the term “mature” refers to the high residence time soot particles in the flame, in contrast to “nascent”, which refers to freshly formed soot.

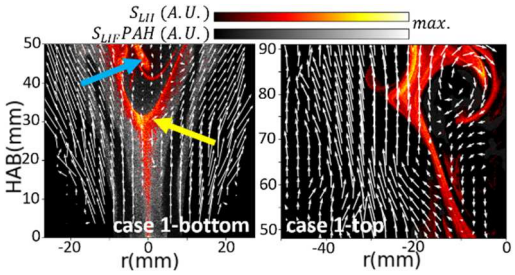

Figure 4: Overlay of instantaneous PAH-PLIF (greyscale) and LII images (colour) for case 1 in the bottom (left) and upper (right) part of the flame.

The region indicated by the yellow arrow in Fig. 4 contains soot arranged in local thin filaments. These filaments arise at the interface between the upper boundary of the zone of PAHs and the lower frontier of the IRZ. Soot particles are then formed due to favourable conditions that promote the inception of soot particles. The weak velocities observed in this area induce large residence times for species, and when combined with a temperature that promotes the chemical decomposition of PAHs, these favour the slow chemistry soot processes [23, 24]. The second area (blue arrow) in which soot is detected is located inside the core of the IRZ, characteristic of a higher velocity in-flow region. Soot is seen in the form of localised, diffuse, thick pockets that are transported by the flow. This is supported by observation of the upper part of the flame in Fig. 4 (right) in which the roll-up of the soot pocket is driven by the orientation of the velocity vectors in this zone.

For all swirl numbers, the formation of soot occurs systematically at the upper frontier of the PAH area, demonstrating that an increase in swirl enables the production of soot at shorter distances from the bluff body. An increase in the swirl intensity also reduces the height at which the temperature-induced decomposition of PAHs is activated, leading to better heating of the fresh gas stream via better penetration of the hot combustion products into the IRZ.

3.3. Soot volume fraction

LII signals were quantified in terms of soot volume fraction using the procedure detailed in section 2.3. The distributions of soot volume fraction (f_v) (Fig. 5) show the measurements for two swirl conditions. Each distribution is composed of stacked slices at two heights.

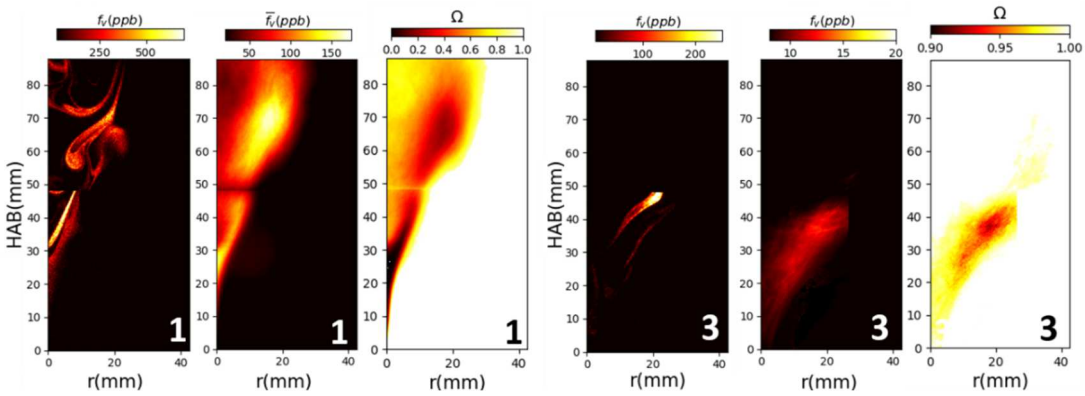

Figure 5: Instantaneous f_v (left), time-averaged f_v(middle) and Ω (right) for conditions 1 and 3.

Sequential instantaneous f_v images show that soot is highly intermittent and spatially isolated. It is obvious that the formation of soot is not a spatially continuous process, despite the fact that soot is observed in the IRZ, where the temperature distributions are known to be fairly homogeneous [6]. A careful observation of the instantaneous f_v distribution recorded at various swirl numbers confirms the results observed in Fig. 4, in which two classes of soot particles are detected. At low swirl, nascent soot particles are formed close to the region in which the consumption of PAHs is observed, while large pockets of soot advected into the IRZ represent mature soot. Furthermore, an increase in the swirl number accelerates the removal of soot circulating in the IRZ, while the nascent particles are preserved.

The intermittency of soot particles can have a strong impact on the interpretation of time-averaged soot volume fraction measurements. Hence, it makes sense not only to work with the average $\overline{f_v}$ but also with the intermittency index (Ω), which allows for the quantification of the soot intermittency in the flame. Intermittency indexes Ω are calculated following [25] and are displayed in Fig. 5 for cases 1 and 3. This parameter is calculated using statistics collected from 1000 instantaneous f_v images. An increase in the swirl number leads to a rise of the turbulence level which is known to be a key factor amplifying the intermittency of soot production [26]. This

phenomenon is illustrated in Fig. 5; the minimum intermittency index observed at low swirl is close to zero, whereas it reaches 0.9 for larger values of swirl. Values of Ω are also relatively large in the IRZ, while low values are found in the area of the nascent soot particles. One of the reasons for this trend is that the region of recirculation of mature soot is dominated by large turbulent eddies that induce a high level of variability in f_v. In contrast, the flow velocity is low in the ISL where nascent soot are formed. The turbulence levels are reduced and residence times are large, thus leading to weaker soot intermittency. It should also be noted that turbulence is not the only physical process governing soot intermittency: the oxidation of soot particles also plays a key role. Soot pockets circulating in the IRZ may be oxidized on the lower side by oxygen molecules contained in the inner stream of the fresh mixture, while the penetration of OH radicals in the upper part of the IRZ will also favour soot oxidation.

For low swirl flames (Fig. 5, case 1), intermittency is very low at the periphery of the IRZ in the regions attributed to nascent soot particles, and increases inside the IRZ due to the phenomena described above. Changing the swirl flow ratio from 0.2 to 0.3 (Fig. 5, case 3) gives a strong global increase in the intermittency, which affects not only the IRZ but also the region of nascent soot with the lowest intermittency indices of 0.9.

3.4. Soot inception, growth, aggregation and oxidation scenario

The combined use of OH-PLIF, PAH-PLIF, PIV and LII results can provide a wealth of information on the formation of soot. The following discussion demonstrates of the importance of combining laser diagnostics to distinguish the processes governing soot formation and consumption. This potential is illustrated in Fig. 6, where overlays of the instantaneous and averaged OH, PAH and soot distributions are plotted for case 2. A detailed observation of these 2D distributions indicates that

several distinct areas, associated with the different steps of soot formation and oxidation, can be identified.

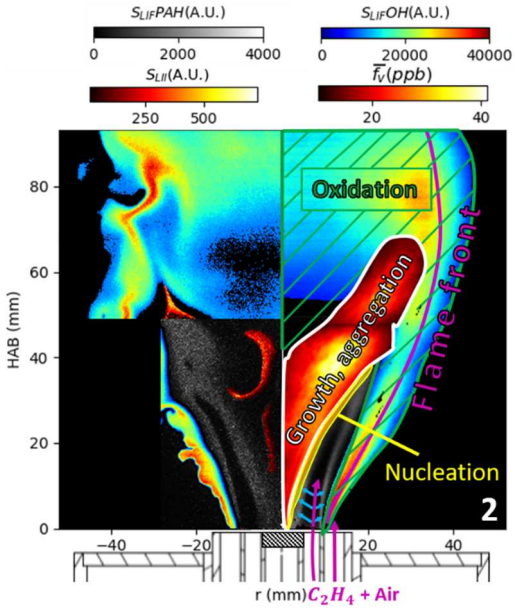

Figure 6: Summary of combined OH-PLIF, PAH-PLIF and LII distributions for case 2: instantaneous distributions (left); time-averaged distributions (right).

The injection of premixed ethylene/air jet streams through the inner and outer tubes is represented by purple arrows. A flame front anchored at the lip of the outer tube develops at the periphery of the reactive flow field. The rich fuel/air mixture escaping from the inner tube prevents any combustion along the centreline of the flame, and no OH production is detected in a large central zone. At the same time, fuel is thermally decomposed into sub-products which then form PAHs in a moderately thick region surrounding the central fuel/air premixed jet. After this region, PAHs are consumed at the upper frontier of the region of PAHs, in favour of a fast production of thin ligaments of nascent soot (yellow area). These soot particles are then advected inside the high-temperature IRZ, where several mechanisms impact the formation of soot. The area outlined in white in Fig. 6 shows the growing and aggregation region, in which a progressive increase of $\overline{f_v}$ with HAB is observed, giving the transition to mature soot particles. The turbulent mixing processes in the core of the IRZ produce high intermittency, as indicated by the high value of the intermittency

index. Downstream from this region, a fast decrease in $\overline{f_v}$ is observed. The origin of this trend stems from the transport of large soot particles into an area where OH radicals are spread inside the IRZ. Fast and full oxidation of these large soot particles therefore occurs, as shown by the null value of $\overline{f_v}$ in this region.

4. Conclusion

PIV, 2D-LII, OH-PLIF and PAH-PLIF diagnostics were used simultaneously to study the formation of soot in swirl stratified premixed C_2H_4/air flames operating at atmospheric pressure. These combined diagnostics allowed for a phenomenological characterisation of the mechanisms of soot formation by simultaneously mapping the aerodynamics, soot volume fraction, flame structure and soot precursors. Various stratification and swirl intensities were used to establish a set of flame conditions that impact the processes of soot production and consumption. Imaging results for OH, PAHs and soot particles indicate distinct regions related to the inception, growth and oxidation of soot. The OH distributions revealed a spatially wrinkled and distributed flame front anchored at the lip of the outer premixed stream, combined with the production of an IRZ. The intensity of the IRZ, which depends on the stratification and swirl levels, plays a key role in the transportation of hot products to the base of the bluff body. At the centre of the flame, the fuel contained in the rich, premixed inner flow stream is rapidly transformed by thermal decomposition into sub-products forming PAHs. The simultaneous imaging of PAHs with soot clearly demarcates the zone in which thin ligaments of nascent soot are formed. Behind this region, a proportion of soot particles is advected into the IRZ, which favours growth and aggregation, and is finally transformed into thick pockets of mature soot. Downstream from this region, fields of OH and mature soot interact. There is then overlap between the OH recirculating in the IRZ and soot pockets, leading to rapid oxidation of soot. Combined with the fluctuations of the velocity inside the IRZ, this produces a high

intermittency of soot production, as confirmed by the intermittency index. Depending on the intensities of stratification and swirl, the interrelationships between the concentrations of OH and PAHs and soot volume fraction are strongly dependent on their respective rates of production and consumption. The combined results from these measurements provide a new and comprehensive database that will be useful for the validation of soot models in swirled and stratified flames.

Acknowledgments

The authors gratefully acknowledge funding from the European Union as part of the SOPRANO H2020 project under Grant Agreement No. 690724.

References

[1] V. Ramanathan, G. Carmichael, Nature Geoscience, 1 (2008) 221.

[2] Z. Klimont, K. Kupiainen, C. Heyes, P. Purohit, J. Cofala, P. Rafaj, J. Borken-Kleefeld, W. Schöpp, Atmos. Chem. Phys., 17 (2017) 8681-8723.

[3] I. Boxx, M. Stöhr, C. Carter, W. Meier, Combustion and Flame, 157 (2010) 1510-1525.

[4] W. Meier, X.R. Duan, P. Weigand, Combustion and Flame, 144 (2006) 225-236.

[5] C. Karagiannaki, G. Paterakis, K. Souflas, E. Dogkas, P. Koutmos, Journal of Energy Engineering, 141 (2015) C4014010.

[6] M.S. Sweeney, S. Hochgreb, M.J. Dunn, R.S. Barlow, Combustion and Flame, 159 (2012) 2912-2929.

[7] H. Koo, M. Hassanaly, V. Raman, M.E. Mueller, K. Peter Geigle, Journal of Engineering for Gas Turbines and Power, 139 (2016).

[8] C. Eberle, P. Gerlinger, K.P. Geigle, M. Aigner, Combustion Science and Technology, 187 (2015) 1841-1866.

[9] B. Zhao, Z. Yang, M.V. Johnston, H. Wang, A.S. Wexler, M. Balthasar, M. Kraft, Combustion and Flame, 133 (2003) 173-188.

[10] M. Frenklach, Physical Chemistry Chemical Physics, 4 (2002) 2028-2037.

[11] M. Frenklach, H. Wang, Symposium (International) on Combustion, 23 (1991) 1559-1566.

[12] R. Puri, R.J. Santoro, K.C. Smyth, Combustion and Flame, 97 (1994) 125-144.

[13] S.-Y. Lee, S.R. Turns, R.J. Santoro, Combustion and Flame, 156 (2009) 2264-2275.

[14] M.S. Sweeney, S. Hochgreb, M.J. Dunn, R.S. Barlow, Combustion and Flame, 159 (2012) 2896-2911.

[15] F. Grisch, M. Orain, AerospaceLab, 1 (2009) p. 1-14.

[16] K. Kohse-Höinghaus, J. Jeffries, Anal. Lett, 32 (1999) 2143.

[17] M. Orain, P. Baranger, C. Ledier, J. Apeloig, F. Grisch, Applied Physics B, 116 (2014) 729-745.

[18] S. Bejaoui, X. Mercier, P. Desgroux, E. Therssen, Combustion and Flame, 161 (2014) 2479-2491.

[19] G.W. Zack, W.E. Rogers, S.A. Latt, Journal of Histochemistry & Cytochemistry, 25 (1977) 741-753.

[20] S. Will, S. Schraml, A. Leipert, Symposium (International) on Combustion, 26 (1996) 2277-2284.

[21] A. Bescond, J. Yon, F.X. Ouf, C. Rozé, A. Coppalle, P. Parent, D. Ferry, C. Laffon, Journal of Aerosol Science, 101 (2016) 118-132.

[22] T. Tanzawa, W.C. Gardiner, Combustion and Flame, 39 (1980) 241-253.

[23] K.P. Geigle, R. Hadef, M. Stöhr, W. Meier, Proceedings of the Combustion Institute, 36 (2017) 3917-3924.

[24] V. Narayanaswamy, N.T. Clemens, Proceedings of the Combustion Institute, 34 (2013) 1455-1463.

[25] M. Roussillo, P. Scouflaire, S. Candel, B. Franzelli, Proceedings of the Combustion Institute, 37 (2019) 893-901.

[26] B. Franzelli, A. Cuoci, A. Stagni, M. Ihme, T. Faravelli, S. Candel, Proceedings of the Combustion Institute, 36 (2017) 753-761.

List of captions

Figure 1: Swirl stratified premixed burner.
Figure 2: Combined instantaneous (left) and time-averaged (right) images of velocity, OH-PLIF, PAH-PLIF and soot distributions. The velocity vectors (instantaneous) and streamlines (time-averaged) represent the axial and radial components.
Figure 3: Combined instantaneous (left) and time-averaged (right) images of OH-PLIF (colour) and PAH-PLIF (greyscale) images.
Figure 4: Overlay of instantaneous PAH-PLIF (greyscale) and LII images (colour) for case 1 in the bottom (left) and upper (right) part of the flame.
Figure 5: Instantaneous fv (left), time-averaged fv(middle) and Ω (right) for conditions 1 and 3.
Figure 6: Summary of combined OH-PLIF, PAH-PLIF and LII distributions for case 2: instantaneous distributions (left); time-averaged distributions (right).

List of supplemental materials

Figure S1: Photographs of flame conditions surveyed in the current study.

Figure S2: Raw image collected on PAH/soot camera

Figure S3: OH-PLIF image

Figure S4: (a): Image obtained with OH masked. (b): Histogram of the image (a) with the threshold determined by the triangle method and the pixel attributed to soot particles and PAH. (c): Resulting soot image. (d): Resulting PAH image.

Figure S5: Comparison between the time-averaged image obtained with 1064 nm excitation LII (right) and 282 nm excitation LII (left).

Figure S6: LII signal recorded on one camera (left), PAH-PLIF signal recorded on the second camera (centre), overlay of both signals (right).